ANNUAL REVIEWS

*Annual Review of Materials Research*

# Modeling Corrosion with First-Principles Electrochemical Phase Diagrams

Liang-Feng Huang,[1] John R. Scully,[2] and James M. Rondinelli[1]

[1]Department of Materials Science and Engineering, Northwestern University, Evanston, Illinois 60208, USA; email: jrondinelli@northwestern.edu

[2]Department of Materials Science and Engineering, University of Virginia, Charlottesville, Virginia 22904, USA

Annu. Rev. Mater. Res. 2019. 49:53–77

First published as a Review in Advance on March 18, 2019

The *Annual Review of Materials Research* is online at matsci.annualreviews.org

https://doi.org/10.1146/annurev-matsci-070218-010105



## Keywords

density functional theory, Pourbaix diagram, corrosion, oxidation, transition metals

## Abstract

Understanding and predicting materials corrosion under electrochemical environments are of increasing importance to both established and developing industries and technologies, including construction, marine materials, geology, and biomedicine, as well as to energy generation, storage, and conversion. Owing to recent progress in the accuracy and capability of density functional theory (DFT) calculations to describe the thermodynamic stability of materials, this powerful computational tool can be used both to describe materials corrosion and to design materials with the desired corrosion resistance by using first-principles electrochemical phase diagrams. We review the progress in simulating electrochemical phase diagrams of bulk solids, surface systems, and point defects in materials using DFT methods as well as the application of these ab initio phase diagrams in realistic environments. We conclude by summarizing the remaining challenges in the thermodynamic modeling of materials corrosion and promising future research directions.

## 1. INTRODUCTION

Materials selection focuses on finding a compound/alloy or composite that exhibits superior properties for a targeted application. Common examples include optimizing mechanical properties for structural materials applications (1–4) and photochemical/chemical reactivities for catalysts and electrodes (5–9). Beyond the primary property of interest, however, the metallurgical and electrochemical stability of the material is another critical factor determining its performance and lifetime in aqueous environments, e.g., marine, biomedical, catalytical, and geological environments (1, 3, 6, 8–15). The ubiquitous battle against materials degradation in industry and government in the form of corrosion accounts for 3 ± 2% of the gross domestic/national product of the countries in the world (16), which clearly demonstrates the economic necessity of corrosion research.

According to data from the *Web of Knowledge* database (17), we have witnessed in the last decade a fast increase in the application of density functional theory (DFT) to corrosion problems (see the DFT + corrosion curve in **Figure 1*a***). Nonetheless, it is still not comparable to the broad application of DFT methods in alloy studies (see the DFT + alloy curve in **Figure 1*a***). For corrosion in a specific field (e.g., alloys), the application of DFT is growing but still in a relatively preliminary stage (see the DFT + alloy + corrosion curve in **Figure 1*a***). Furthermore, according to the *World Population Ageing 2017* report published by the United Nations (18), the aged population will double within 30 years (**Figure 1*b***, inset), which indicates that artificial biomedical implants to replace degraded bones will increase at a high rate over that period. Although the corrosion behaviors and toxicities of alloy implants in in vivo environments have been studied intensively for decades (3, 10, 12, 19–25), the use of DFT approaches to solve biomedical problems remains in its infancy (**Figure 1*b***). To that end, we explain and review DFT approaches to understanding materials corrosion in broad areas of materials research while highlighting recent significant achievements in using these first-principles methods.

The corrosion behaviors of materials, such as metallic alloys, are always determined by various intrinsic drivers—composition, nanostructure, morphology, and defects—of metal substrates and

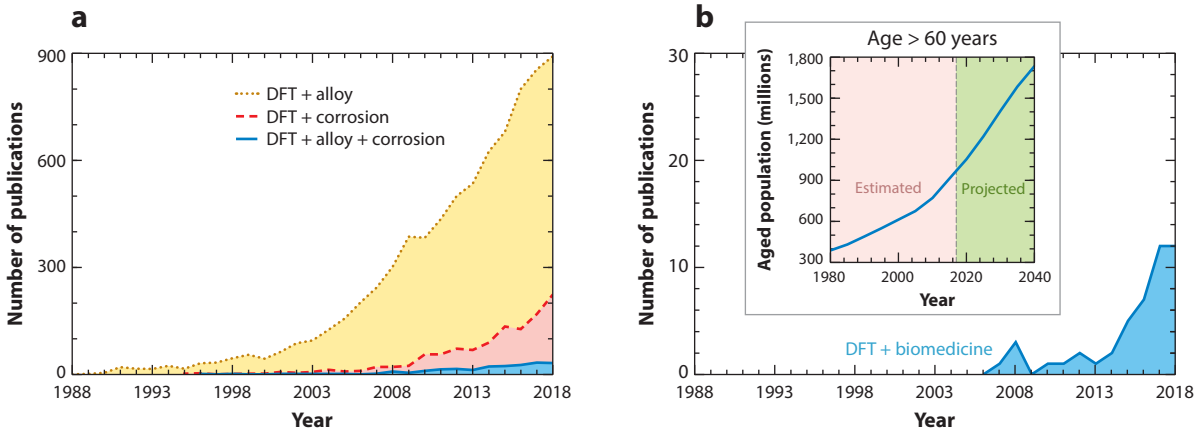


**Figure 1**

(*a*) The number of publications from 1988 to 2018 according to the *Web of Knowledge* database (17) (by Clarivate Analytics 2018, **http://apps.webofknowledge.com**) with keywords of density functional theory + alloy + corrosion, density functional theory + corrosion, and density functional theory + alloy. (*b*) The number of publications searched with keywords of density functional theory + biomedicine. The inset shows the estimated/projected world aged populations in different years. Data from the *World Population Aging 2017* report by the United Nations (18). The numbers of publications in 2018 in panels *a* and *b* are projected on the basis of the data for the first half of 2018.

passivating layers and extrinsic environmental factors or dependencies—voltage bias, electrolyte solution, and temperature—as well as the possible interactions among all of these factors (13, 26–29). Electrochemical phase diagrams with respect to many ubiquitous environmental parameters (e.g., solution pH, electrode potential, aqueous ion concentration, dissolved gases, complex agents, and temperature) can be used to effectively understand and predict many stability trends of materials under complex and variable corrosion environments, including reduction, oxidation, and dissolution trends (30–37). It is challenging for experimental approaches to disentangle the roles of different factors and mechanisms in the complex process of corrosion. In addition, it is difficult to construct electrochemical phase diagrams by direct and comprehensive measurements owing to challenges in controlling all environmental conditions, in controlling kinetic factors, and in probing at the relevant length scales and timescales the cooperating and competing microscopic mechanisms. In such scenarios, DFT calculations are a promising alternative method to disentangle and identify important microscopic mechanisms while predicting useful phenomena. The success of DFT relies on its accuracy (the error should be within the chemical threshold of $\sim 10^{-2}$ eV per atom) and its capability (there should be feasible approaches available to deal with complex cases), which are the main reasons why the DFT community has maneuvered into the materials corrosion field.

In the following, we review important basic principles for electrochemical phase diagrams of materials and the use of DFT to obtain the free energies that are required in the simulation of electrochemical stabilities. Then, we discuss developments in state-of-the-art DFT-based simulation methods for constructing electrochemical phase diagrams of different bulk and defective systems, including transition metals and their compounds, solid surfaces and the adsorbates on them, and defects in oxides. The impact of these DFT methods on the materials corrosion field is demonstrated using realistic examples. Last, we describe key challenges and opportunities for the future application of DFT methods to materials corrosion.



## 2. PRINCIPLES OF ELECTROCHEMICAL PHASE DIAGRAMS

### 2.1. Pourbaix Diagrams

The electrochemical phase diagrams of materials with respect to solution pH and electrode potential ($U_p$) were first established by Marcel Pourbaix (30) and are thus termed Pourbaix diagrams. There are also many derivatives of a Pourbaix diagram, e.g., chemical stability diagrams, speciation diagrams, and predominance diagrams (30, 38, 39), which are used to describe the stability of materials under various electrochemical conditions. Although these diagrams present the electrochemical stabilities of the involved species in manners that differ from the Pourbaix diagram, the processes to model them are similar and require the same energies and electrochemical formula as input. For that reason, we limit our discussion to the DFT simulation of Pourbaix diagrams. Pourbaix diagrams map the phase domains corresponding to metals, oxides, hydroxides, oxyhydroxides, and aqueous ions within the considered ranges of pH (e.g., $\in [-2, 16]$) and $U_p$ (e.g., $\in [-3, 3]$ V), as shown by the Ti Pourbaix diagram in **Figure 2**. In Pourbaix diagrams, the standard hydrogen electrode (SHE) is used as the potential reference (30), where 0 V corresponds to the electrode potential for $H_2$ evolution at $[H^+] = 1$ M (pH = 0). SHE is a convenient reference electrode for simulating the electrochemical energies and phase diagrams, although many other kinds of reference electrodes, which rely on other redox reactions, are actively used in electrochemical experiments (40) (see sidebar titled Reference Electrode Potentials).

Pourbaix diagrams find prototypical use in predicting the stabilities of materials used in photocatalysts and electrochemical catalysis, because they can help reveal the corrosion resistance of these catalysts under some possible operating conditions, e.g., $TiO_2$ under solar irradiation. $TiO_2$

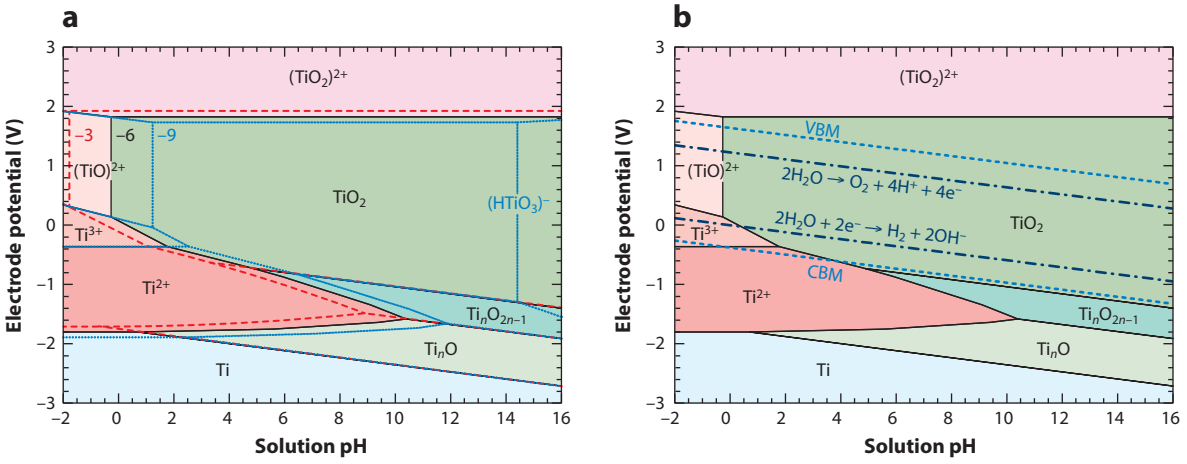


**Figure 2**

Calculated Ti Pourbaix diagrams using density functional theory (DFT) with Heyd-Scuseria-Ernzerhof (HSE)-type screened Hartree-Fock exchange. (*a*) Ti Pourbaix diagrams at aqueous ion concentration [*I*] of $10^{-3}$ M (*red dashed line*), $10^{-6}$ M (*black solid line*), and $10^{-9}$ M (*dotted blue line*). (*b*) Ti Pourbaix diagram (at $[I] = 10^{-6}$ M) with the positions of the valence band maximum (VBM) ($U_p = 1.64 - 0.059 \cdot \text{pH}$) and conduction band minimum (CBM) ($U_p = -0.38 - 0.059 \cdot \text{pH}$) of rutile $TiO_2$, as well as the phase boundaries for water oxidation (upper, $U_p = 1.23 - 0.059 \cdot \text{pH}$) and water reduction (lower, $U_p = -0.059 \cdot \text{pH}$). Vibrational free energies are included and efficiently calculated at the DFT-PBEsol (Perdew-Burke-Ernzerhof revised for solids) level in both panels *a* and *b*. Figure adapted with permission from Reference 41. Copyright 2015, American Physical Society.

is a superior catalyst for water splitting and organic contaminant decomposition (41), and the stability of these properties can be gleaned from the relative positions of its dissolution boundaries, the valence band maximum (VBM) and conduction band minimum (CBM), and the stability boundaries of water (or an organic contaminant to decompose) in the Pourbaix diagram

## REFERENCE ELECTRODE POTENTIALS

In addition to the standard hydrogen electrode (SHE), other reference electrodes include the following:

- Saturated calomel electrode (SCE) ($Hg/Hg_2Cl_2$ electrode): The reference potential is higher than SHE by 0.241 (0.244) V in saturated KCl (saturated $Hg_2Cl_2$) and at 25°C.
- Silver chloride electrode (Ag/AgCl): The reference potential is higher than SHE by 0.197 V in saturated KCl and at 25°C.
- Copper–copper sulfate electrode (CSE) (Cu/saturated $CuSO_4$): The reference potential is higher than SHE by 0.314 V at 25°C.
- Mercury–mercurous sulfate electrode (MSE) ($Hg/Hg_2SO_4$): The reference potential is higher than SHE by 0.640 V in saturated $K_2SO_4$ and at 25°C.
- Silver–silver sulfate electrode (SSE) ($Ag/Ag_2SO_4$): The reference potential is higher than SHE by 0.680 V in saturated $K_2SO_4$ and at 25°C.
- Reversible hydrogen electrode (RHE): The pH-dependent reference potential is lower than SHE by $0.0592 \cdot \text{pH}$.

Many water electrolysis experiments use the RHE as a natural reference because the equilibrium is established quickly and because the reaction is quite reversible and constant with time and maintains zero electrode potential at any temperature.

(**Figure 2*b***). The positions of the VBM and CBM are always within the phase domain of $TiO_2$ but are fully beyond that of the water redox values. This means that $TiO_2$ will be stable under both (*a*) an open circuit potential generated by VBM–CBM electronic excitations and (*b*) the electrode potentials for the evolutions of $H_2$ and $O_2$ gases (i.e., water electrolysis occurs). This aforementioned electrochemical analysis to describe photocatalyst stability can be readily transferred to predict the effects of electromagnetic irradiation on materials corrosion from simulated Pourbaix diagrams. A key aspect for this analysis is that the relative positions of the VBM and CBM are accurately calculated, which is now possible using advanced exchange-correlation functionals to DFT (42–47). Furthermore, metastable materials can also be studied using Pourbaix diagrams, with the most stable materials phases excluded in the simulated phase diagram. Such metastable Pourbaix diagrams can help in understanding and predicting precipitation reactions and the transient formation of intermediate phases in realistic situations in which rates become important (48, 49).

## 2.2. Navigating Pourbaix Diagrams

Pourbaix diagrams typically exhibit phase space that is partitioned among three general domains: an immunity domain where the metal/alloy is stable; a passivation domain defined by, for example, the associated oxides and hydroxides; and a corrosion domain with aqueous ions in solution. The characters of the phase boundaries separating these domains in Pourbaix diagrams are determined by the mechanisms of the corresponding transitions. Four types of phase boundaries appear in Pourbaix diagrams, as shown in the Ti Pourbaix diagram (**Figure 2**) and described next. In addition, the boundary lengths and positions are determined by the formation energies; for this reason, variations in Pourbaix diagrams are expected when variations in the accuracy of such energies are large.

**2.2.1. Horizontal phase boundary.** A transition between two materials' phases will appear as a horizontal phase boundary when there is a change only in the cation valence but not in the number of anions (oxide ions), e.g., the reactions of $Ti \rightarrow Ti^{2+} + 2e^-$, $Ti^{2+} \rightarrow Ti^{3+} + e^-$, and $TiO_2 \rightarrow (TiO_2)^{2+} + 2e^-$. The reaction chemical potential $\Delta\mu$ (in electron volts) can be expressed as

$$\Delta\mu = \mu_p - \mu_r - n_e e U_p,$$

where $\mu_p$ and $\mu_r$ are the chemical potentials of the product and reactant, respectively, and $n_e$ is the number of evolved electrons, i.e., the number of electrons to complete the half-cell reaction at a single time (equal to the increase in cation valence). In these two reactions, the products [$Ti^{2+}$ and $(TiO_2)^{2+}$] are the oxidized species being compared to their corresponding reactants (Ti and $TiO_2$, respectively), whereas in the reactions discussed below, the reactants may be more oxidized than or have the same cation valences as the products. When the energy unit of kilojoules per mole is used instead of electron volts, the constant $e$ should be replaced by the Faraday constant $F$ ($= eN_A = 9.649 \times 10^5$ C mol$^{-1}$, where $N_A$ is the Avogadro constant $6.022 \times 10^{23}$ mol$^{-1}$), which is also the same for the following related formula. At the condition of $\Delta\mu = 0$, the derived critical electrode potential $U_p = (\mu_p - \mu_r)/(n_e e)$ is thus independent of solution pH, resulting in the horizontal phase boundary.

**2.2.2. Vertical phase boundary.** A vertical phase boundary corresponds to a phase transition without a change in oxidation state of the cation, e.g., the reactions of $TiO^{2+} + H_2O \rightarrow TiO_2 + 2H^+$ and $TiO_2 + H_2O \rightarrow (HTiO_3)^- + H^+$. The associated reaction chemical potential $\Delta\mu$ (in

electron volts) can be expressed as

$$\Delta\mu = \mu_p - \mu_r - \mu_{H_2O} - n_H k_B T \ln(10)\cdot pH,$$

where, $\mu_{H_2O}$ is the standard chemical potential of water and $n_H$ is the number of $H^+$ ions produced in the reaction. When the energy unit of kilojoules per mole is used instead of electron volts, the Boltzmann constant $k_B$ should be replaced by the gas constant $R$ ($= N_A k_B = 8.314\,J\,mol^{-1}\,K^{-1}$). At $\Delta\mu = 0$, the derived critical solution pH $[(\mu_p - \mu_r - \mu_{H_2O})/(n_H k_B T \ln(10)]$ is independent of $U_p$, resulting in a vertical boundary at this pH.

**2.2.3. Positive-slope phase boundary.** When the cation valence decreases but the number of anions increases in a phase transition, the phase boundary will have positive slope $dU_p/dpH > 0$. In **Figure 2**, this corresponds to the reactions of $Ti^{2+} + xH_2O + 2(1-x)e^- \rightarrow TiO_x + 2xH^+$ and $(TiO_2)^{2+} + H_2O + 2e^- \rightarrow (HTiO_3)^- + H^+$, where $x$ is the O/Ti ratio in the interstitial Ti oxides ($Ti_nO$, $x = 1/n < 1$). For these transitions,

$$\Delta\mu = \mu_p - \mu_r - n_{H_2O}\mu_{H_2O} + n_e e U_p - n_H k_B T \ln(10)\cdot pH,$$

where $n_{H_2O}$ and $n_e$ are the numbers of $H_2O$ and electrons on the reactant side of the reaction, respectively. At $\Delta\mu = 0$, the derived critical $U_p$ is dependent on pH with a positive slope of $dU_p/dpH = \frac{n_H}{n_e e} k_B T \ln(10) > 0$.

**2.2.4. Negative-slope phase boundary.** The slope $dU_p/dpH$ of a phase boundary is negative when both the cation valence and the anion number synchronously increase in the reaction. Such phase boundaries are the most abundant type to appear in Pourbaix diagrams, because the solution becomes more oxidizing with increasing pH. In other words, atomic oxygen has a lower stability in a less acidic (or more alkaline) solution, which is expressed as

$$\mu_O = \mu(H_2O) - 2\mu_{H^+} - 2\mu_{e^-} = \mu_{H_2O} + 2eU_p + 2k_B T \ln(10)\cdot pH. \quad 1.$$

Thus, a material tends to be further oxidized (i.e., to a higher cation valence) with increasing pH of the solution. The typical reactions are $Ti + xH_2O \rightarrow TiO_x + 2xH^+ + 2xe^-$ (electrochemical metal oxidation) and $Ti^{2+} + 2H_2O \rightarrow TiO_2 + 4H^+ + 2e^-$ (electrochemical oxide precipitation), where the $TiO_x$ can be an interstitial oxide ($Ti_nO$, $x = 1/n < 1$) or a Magnéli oxide ($Ti_nO_{2n-1}$, $x = (2n-1)/n \in [1, 2]$). The reaction chemical potentials are expressed as

$$\Delta\mu = \mu_p - \mu_r - n_{H_2O}\mu_{H_2O} - n_e e U_p - n_H k_B T \ln(10)\cdot pH.$$

The derived critical $U_p$ at $\Delta\mu = 0$ is dependent on pH with slope $dU_p/dpH = -\frac{n_H}{n_e e} k_B T \ln(10) < 0$.

## 2.3. Additional Considerations

Apart from $U_p$ and pH, many other environmental factors are also critical for assessing the electrochemical stability of materials; these factors include solution composition, aqueous ion concentration [$I$], and temperature (30–37, 50–52). The variations of Pourbaix diagrams with respect to these parameters can provide much useful information about materials performance and behavior under realistic electrochemical environments. Some related principles and examples using these additional considerations are described below.

The stability, manifesting as the phase area, of aqueous ions always decreases with increasing $[I]$ (30), which is well exemplified by the reduction in the phase areas of $Ti^{2+}$, $Ti^{3+}$, and $(TiO)^{2+}$ in the Ti Pourbaix diagram in **Figure 2*a*** ($[I] \in [10^{-9}, 10^{-3}]$ M). This trend can be understood from the expression of $\mu_I$ (53) given by $\mu_I([I]) = \mu_I^0 + k_B T \ln([I])$, where $\mu_I^0$ (in electron volts) is the chemical potential at the standard concentration (i.e., 1.0 M). Here $[I]$ is used to approximate the aqueous ion activity. At a higher $[I]$, the aqueous ions become more crowded and are then less stable in solution (i.e., have higher $\mu_I$), making it easier to extract them out of solution to form condensed (solid) materials.

In some situations [e.g., nuclear facilities (54)], the active solid-state materials will be in contact with high-temperature solutions. Researchers have used some efficient empirical models to obtain the temperature-dependent chemical potentials of solids and aqueous ions by extrapolating from the free energies at low temperatures, and those temperature-dependent chemical potentials are then used to produce temperature-dependent Pourbaix diagrams (31–33, 36, 50–52). With increasing temperature, some oxides (e.g., NiO and $Cr_2O_3$) may become more stable, indicating their enhanced growth on related metal surfaces by heating (31–33, 51, 52). In contrast, $TiO_2$ and $Ni(OH)_2$ have lower electrochemical stabilities (32, 52), indicating possibly severe corrosion issues in hot water for both these compounds and the metal substrates that they are protecting. In addition, the stability of $Fe_2O_3$ is enhanced by heating at $[I] = 10^{-6}$ M but is weakened at $[I] = 10^{-8}$ M (31), while the stability of $Co(OH)_2$ is weakened at $[I] = 10^{-6}$ M and enhanced only at a high $[I] = 10^{-2}$ M (50). Therefore, the thermal effects on the electrochemical stability (corrosion behavior) of materials depend sensitively on the type of material and environmental conditions. To quantitatively understand and predict the temperature-dependent electrochemistry with high accuracy, more advanced theoretical calculations, such as those based on DFT, and comparative experimental measurements are required in the future.

In various realistic environments, the solution usually exhibits a complex chemical composition in which many corrosive agents may coexist; for example, $Cl^-$, $SO_4^{2-}$ in seawater and protein/sugar molecules in vivo in the human body are active (10, 12, 19–21, 23, 24, 28). To account for the effects of these environmental agents, the reactions of these agents with the materials under study should be additionally considered when simulating electrochemical stabilities (34, 35, 37). For complex aqueous ions and solid compounds, both state-of-the-art DFT calculations and experimental measurements on their electrochemical behaviors are also largely lacking, which may impede the assessment of model accuracies with the aim of designing novel materials (55) operating under realistic conditions from first principles.

## 2.4. Pourbaix Diagrams from Density Functional Theory

The application of DFT for simulating Pourbaix diagrams is depicted by the workflow shown in **Figure 3**. This DFT workflow consists of three major parts:

1. formulation of the needed reaction chemical potentials ($\Delta\mu$);
2. collection of the experimental standard chemical potentials of aqueous ions ($\mu_I^0$); and
3. calculation of the formation free energies ($\Delta_f G$, or standard chemical potentials) of solids, including vibrational contributions.

The constructed formula and collected or calculated energies are then combined together to assess the relative stabilities of all the materials phases at each electrochemical condition (in terms of pH and $U_p$). After scanning through the phase space of interest and determining the stable compound or ion at a given pH and $U_p$ pair, one can finally generate the Pourbaix diagram.

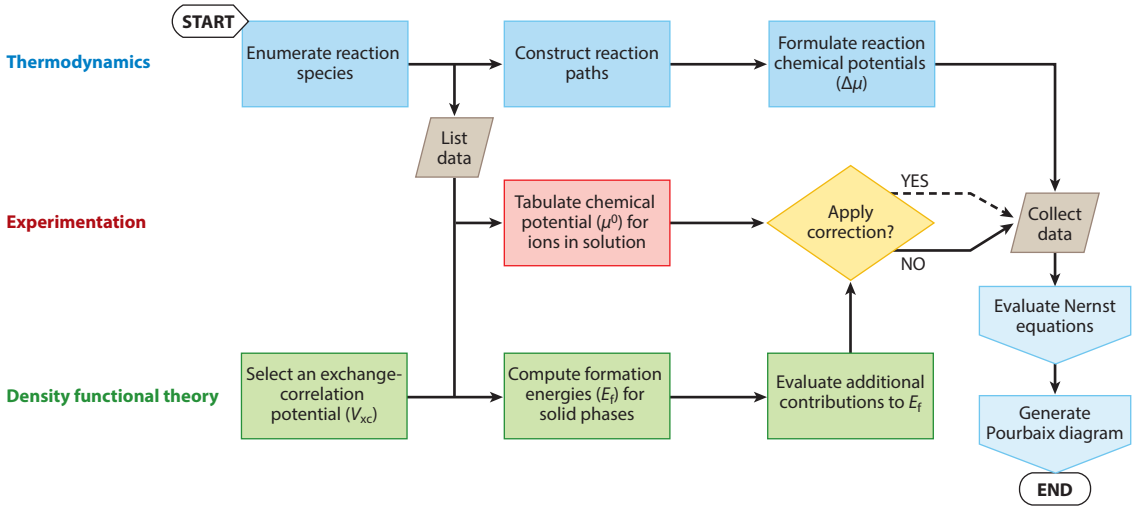


**Figure 3**

Workflow chart describing how one can simulate Pourbaix diagrams using density functional theory (DFT) free energies of formation for solid compounds. Most DFT simulation approaches follow this workflow, with the main difference among implementations concerning whether or not the DFT energies are modified in some way as indicated in the box "Apply correction?". Following the box "Apply correction?", the solid arrow and the dashed arrow indicate the avoidance and usage, respectively, of ad hoc energetic corrections to the DFT energies. Adapted with permission from Reference 41. Copyright 2015, American Physical Society.



In many previous Pourbaix diagrams (30–37, 50–52), only the experimental chemical potentials for both solid compounds and aqueous ions were used. However, investigations of the available databases for experimental energies (30–33, 56–60) revealed that, although the experimental energies for regular aqueous ions—such as $M^{2+/3+}$, where $M$ is a 3*d* transition metal ranging from Cr through Ni—exhibit quite small deviations among different databases (e.g., usually at ∼0.02 eV and infrequently at ∼0.1 eV), the experimental data for solid-state compounds always exhibit large deviations [e.g., ∼0.3–1.6 eV per formula unit for many oxides and (oxy)hydroxides of these metals]. This large uncertainty in the experimental energies usually originates from the measurement methods [e.g., combustion (60)] used to derive the formation free energies of solid compounds. For example, during a combustion process, many inevitable technical and often unintentional physical issues arise that tend to lend uncertainty to the free energies (41, 48); these factors include uncontrollable (inhomogeneous) temperature, defect generation and contamination, mass loss, and heat measurement error. For example, the high concentration of defects makes NiO samples synthesized by the flame-fusion method (61) appear blackish in color, in contrast to the well-known greenish color for pristine NiO. In addition, it is important to point out here that the Pourbaix diagrams for some materials using experimental energies can be inconsistent with various electrochemical phenomena directly observed at low (room) temperature, which is further discussed in Section 3. As a state-of-the-art computational method, DFT is expected to become an alternative approach for obtaining accurate energies for solid-state materials and facilitating reliable Pourbaix diagram generation.

**LDA:** local density approximation

**GGA:** generalized-gradient approximation

Since the birth of DFT in 1964 (62, 63), there have been various density functionals proposed to approximate the exact nonlocal electronic exchange and correlation, with the aim of calculating materials properties accurately in efficient or tractable ways (64–66). There are local local density approximation (LDA) functionals (67, 68), semilocal generalized-gradient approximation (GGA)

functionals [e.g., Perdew-Burke-Ernzerhof (PBE) (69) and Perdew-Burke-Ernzerhof revised for solids (PBEsol) (70)], metaGGA functionals [e.g., Tao-Perdew-Staroverov-Scuseria (TPSS) (71), revised TPSS (revTPSS) (72), made simple (MS2) (73), and strongly constrained and appropriately normed (SCAN) (74)] with the electronic kinetic energy used to describe the nonlocal electronic exchange, and hybrid functionals [e.g., B3LYP (75, 76), PBE exchange mixed with 25% Hartree-Fock (HF) exact exchange (PBE0) (77), and Heyd-Scuseria-Ernzerhof with screened HF exchange (HSE) (78–81)] with nonlocal electronic exchange partially included. The description of exchange and correlation effects improves upon going from LDA to GGA, metaGGA, and the hybrid methods, and the theoretical accuracy generally (but not always) increases. In contrast, the computational expense increases considerably; e.g., the metaGGA (hybrid) method requires one order (two orders) of magnitude more CPU hours than do the conventional LDA and GGA methods. Additional details of the intricacies of and advances in density functional methods can be found in References 82 and 83.

For materials with strong electronic correlation (e.g., transition metal oxides), a DFT implementation using a static mean-field on-site Hartree-Fock approximation through the so-called DFT plus Hubbard $U$ (DFT + $U$) method (84, 85) is also frequently used to calculate the electronic structure accurately with an efficiency equivalent to that of GGA functionals. The addition of the parameter $U$ changes the reference of the electronic potential, and the as-calculated electronic energy always increases with increasing $U$, resulting in a likely underestimation of the formation energy for correlated oxides. To solve this DFT + $U$ complication, an ad hoc correction to diatomic $O_2$ (86–89) or the metal elements (90, 91) should be used to lower the compound formation energy. Finally, in this approach, the reported experimental energies are then used as criteria to fit the $U$ value, in the presence of that ad hoc correction.

When DFT + $U$ are used for electrochemical situations (53), the chemical potentials of aqueous ions also need additional ad hoc corrections to make the dissolution energies of oxides comparable to those of the experimental data. These energetic corrections involved in the DFT + $U$ calculations correspond to the box "Apply correction?—Yes" in the workflow diagram in **Figure 3**. The high efficiency of DFT + $U$ makes it possible to calculate the Pourbaix diagrams of a large number of materials in a high-throughput manner (49, 53, 92) and in complicated nanoparticle systems (93, 94).

An alternative to the DFT + $U$ method and its many accompanying ad hoc energetic corrections is to use the ab initio DFT method and a correction-free approach (see the box "Apply correction?—No" in **Figure 3**). This approach can be realized when one chooses an accurate density functional [see the box "Select an exchange-correlation potential ($V_{xc}$)" in **Figure 3**], which makes the calculated thermodynamic energies for solid compounds free of any influence by the existing experimental data—at this point the scheme becomes fully first principles. As mentioned above, the experimental energies may be inaccurate with errors ranging from 0.3 to 1.6 eV/f.u. for many transition metal compounds (oxides, hydroxides, and oxyhydroxides), and such experimental error will be transferred into the theoretical simulation when using DFT + $U$. In other words, DFT energies are "corrected" to fit inaccurate data. Thus, a correction-free original DFT approach is preferred. Furthermore, the correlated electronic interactions are sometimes oversimplified by the mean-field on-site model in DFT + $U$, which fails for many materials with delocalized or nonlocal electronic correlation and high-degree orbital hybridizations (95). In contrast, these complex electronic interactions may be well captured by the metaGGA and hybrid methods with nonlocal electronic potentials. A comprehensive evaluation and understanding of the performances of different DFT methods for simulating electrochemical properties of different materials classes still require much computational effort in the future.

**PBE:** Perdew-Burke-Ernzerhof

**PBEsol:** Perdew-Burke-Ernzerhof revised for solids

**TPSS:** Tao-Perdew-Staroverov-Scuseria

**revTPSS:** revised TPSS

**MS2:** made simple

**SCAN:** strongly constrained and appropriately normed

**PBE0:** PBE exchange mixed with 25% Hartree-Fock (HF) exact exchange

**HSE:** Heyd-Scuseria-Ernzerhof with screened HF exchange

## 3. ELECTROCHEMICAL PHASE DIAGRAMS OF BULK MATERIALS

Here we discuss the application of the correction-free first-principles approach (**Figure 3**) for Ni and Fe Pourbaix diagrams. The DFT-calculated Ni Pourbaix diagram (48, 95) systematically explains various electrochemical observations appearing both over the past few decades and more recently with modern electrochemical measurements. Studies comparing these DFT diagrams with traditional Pourbaix diagrams obtained using experimental free energies of formation $\Delta_f G$ for solid compounds suggest that it is more meaningful to compare simulated Pourbaix diagrams with electrochemical observations rather than with derived phase diagrams. The success in understanding the Ni Pourbaix diagram has motivated studies of the Fe Pourbaix diagram (96), which is of especially high importance for the corrosion field. The DFT-based Fe Pourbaix diagram is also consistent with many electrochemical measurements and has helped revise the interpretation of some recent X-ray diffraction (XRD) results for Fe samples with corrosion-resistant polymer coatings (97, 98). Furthermore, both the Ni and Fe Pourbaix diagrams have broad implications; they are useful for explaining many fluid-driven phenomena active during the evolution of Earth's crust (15).

### 3.1. Improved Ni Pourbaix Diagrams

**Figure 4*a*** shows the electronic energies of formation ($\Delta_f E_e$) for Ni oxides, hydroxides, and oxyhydroxides calculated using various DFT methods (LDA, PBE, PBEsol, revTPSS, MS2, and HSE) (95). It is well known that the most stable oxide under ambient conditions is NiO (48), and only MS2 and HSE reproduce NiO to be the correct lowest-energy phase. The dramatic differences between the $\Delta_f E_e$ values from different DFT methods also indicate the important role of nonlocal electronic exchange in calculating accurate thermodynamic energies for materials with localized 3*d* electrons (95). The free energies of formation ($\Delta_f G$) at the standard atmosphere condition (i.e., 298.15 K and 1 bar) from MS2 and HSE are compared with the experimental values in **Figure 4*b***, and these values deviate from each other. It can also be seen that the HSE and experimental $\Delta_f G$

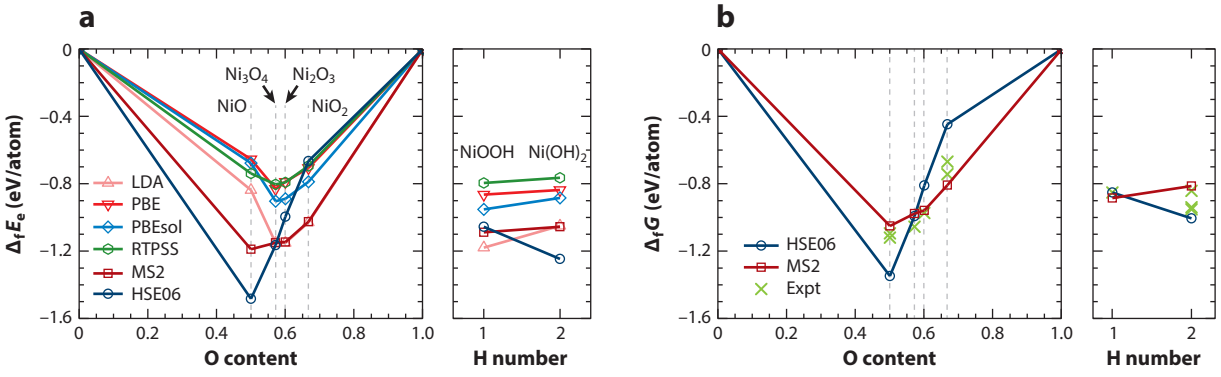


**Figure 4**

(*a*) Electronic energies of formation ($\Delta_f E_e$) for various Ni compounds calculated using different DFT methods and (*b*) free energies of formation ($\Delta_f G$) from the MS2 and HSE06 methods, where the expt $\Delta_f G$s are compared. In each case, the level of DFT at which the electronic energies are calculated is given by the method specified, and the vibrational free energies at room temperature are obtained using only the DFT-PBEsol method since the vibrational energies are less dependent on the selected exchange-correlation functional. Abbreviations: DFT, density functional theory; expt, experimental; HSE, Heyd-Scuseria-Ernzerhof with screened Hartree-Fock exchange; LDA, local density approximation; MS2, made simple; PBE, Perdew-Burke-Ernzerhof; PBEsol, Perdew-Burke-Ernzerhof revised for solids; RTPSS, revised Tao-Perdew-Staroverov-Scuseria. Adapted with permission from Reference 95. Copyright 2017, IOP Publishing.

values present similar qualitative chemical trends in oxides and (oxy)hydroxides, despite the considerable quantitative difference of $\lesssim$0.3 eV/atom.

The Ni Pourbaix diagrams simulated using the HSE and experimental $\Delta_f G$ values at a moderate [*I*] of $10^{-6}$ M are shown in **Figure 5*a*,*b***. All Pourbaix diagrams using the $\Delta_f G$ values by other

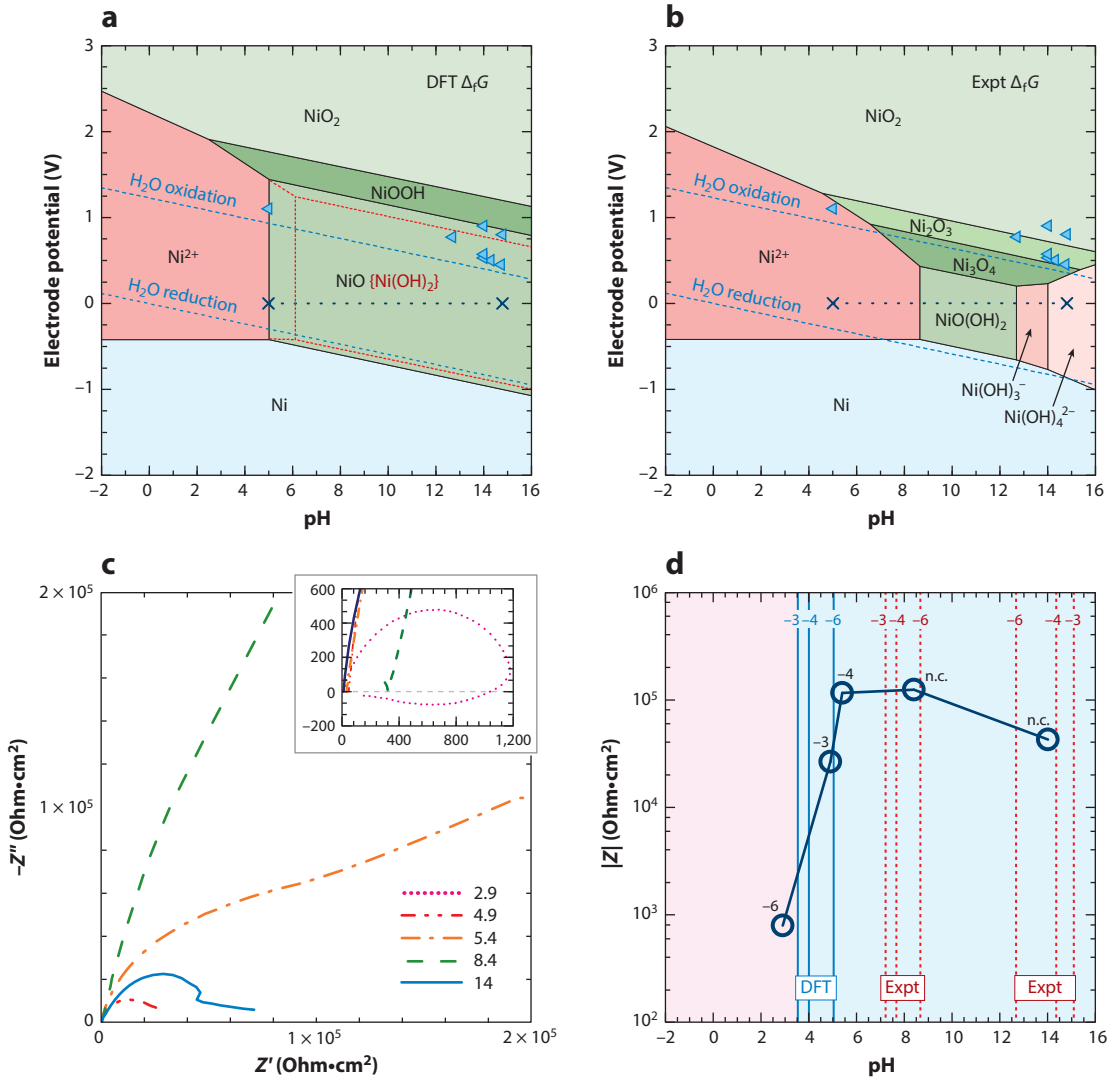


**Figure 5**

Ni Pourbaix diagrams (at room temperature and $[I] = 10^{-6}$ M) simulated using (*a*) density functional theory (DFT) and (*b*) experimental (expt) free energies of formation ($\Delta_f G$), where the pH range for stability against dissolution (*cross-capped dotted blue line*) and oxidation potentials (*blue triangles*) of $Ni(OH)_2$ and NiO are indicated, and (*c*,*d*) the direct expt measurements of the electrochemical impedances for the Ni samples exposed to solutions at pH values ranging from 2.9 to 14 and [*I*] values ranging from $10^{-6}$ to $10^{-3}$ M or not controlled (n.c.). The Nyquist plots (voltage frequency $\omega = 10^5 \sim 10^{-3}$ Hz) of the measured electrochemical impedances are shown in panel *c*. The inset in panel *c* enlarges the result at pH = 2.9. The measured pH-dependent |*Z*| (at $\omega = 10^{-2}$ Hz) is shown in panel *d*, which is compared with the simulated dissolution boundaries of NiO using the DFT and expt $\Delta_f G$ values. Adapted with permission from Reference 48. Copyright 2017, American Chemical Society.

DFT methods (95) incorrectly indicate unstable NiO and $Ni(OH)_2$ due to the underestimated electronic/free energies of formation (**Figure 4*a*,*b***). Because DFT-HSE calculations show that NiO is more stable than $Ni(OH)_2$ by 0.13 eV under electrochemical conditions, NiO is excluded in the modeling of the phase diagram to reveal the phase domain of the metastable $Ni(OH)_2$, as shown in **Figure 5*a***. The first-principles Pourbaix diagram can explain many known electrochemical phenomena not accounted for in the experimental diagram obtained from the experimental energies (48):

- NiO and $Ni(OH)_2$ have very similar electrochemical stabilities, which explains their ubiquitous coexistence in electrochemical conditions. Upon immersion of a Ni electrode into a solution, although the $Ni(OH)_2$ passivating layer always forms quickly on the surface, due to its higher kinetic activity it is always followed by a slower $Ni(OH)_2$–NiO transformation and the continuous formation of a NiO layer underneath. These behaviors indicate the relatively higher electrochemical stability of NiO. This behavior is consistent with the DFT result but contradicts the known diagram simulated using experimental $\Delta_f G$s.
- NiO and/or $Ni(OH)_2$ should be stable in solutions at pH $\gtrsim$ 5, which is consistent with the DFT-based Ni Pourbaix diagram. In contrast, the experiment-based diagram considerably underestimates the stability domain at pH values ranging from 8.7 to 12.7.
- The $Ni(OH)_2$–NiOOH transition is an important process for the electrolysis of water, and the transition potential has been measured to be between 0.5 and 1.0 V at pH $\sim$ 14. This is consistent with the phase boundary at 0.75 V in the presented DFT-HSE-based Pourbaix diagram, while in the experiment-based diagram, NiOOH is not even stable. (Note that DFT Pourbaix diagrams constructed from local density functionals would also incorrectly locate the boundary.)

To further assess the accuracy of the DFT-based Pourbaix diagram, electrochemical impedance spectroscopy was performed to measure the formation of NiO and $Ni(OH)_2$ on Ni electrodes exposed to various buffered solutions at pH values ranging from 2.9 to 14 (48). The measured frequency-dependent impedances (real part $Z'$ and imaginary part $Z''$) and the absolute impedances ($|Z|$) at a low frequency are shown in **Figure 5*c*,*d***. The $|Z|$–pH relationship clearly indicates that the dissolution boundary of the passivating layer should reside at a pH between 3 and 5, which is consistent with the DFT phase boundaries of NiO and $Ni(OH)_2$, while the experimental $\Delta_f G$ values lead to incorrect locations of these boundaries. In addition, surface-enhanced Raman spectroscopy has been used to characterize the passivating layer on Ni, confirming the coexistence of NiO and $Ni(OH)_2$ (48).

## 3.2. Improved Fe Pourbaix Diagrams

The Fe Pourbaix diagrams simulated at the DFT-HSE level (at a moderate $[I] = 10^{-6}$ M) and the experimental $\Delta_f G$ values are shown in **Figure 6*a*,*b***and are reproduced from Reference 96. There are two major differences between the DFT- and experiment-based diagrams: (*a*) $Fe_3O_4$ dominates over $Fe_2O_3$ in the DFT diagram, while it is reversed in the experimental one, and (*b*) the oxide has a lower dissolution pH value in the DFT diagram. These dramatic differences make it possible (and straightforward) to assess the reliability of the two diagrams by using available experimental observations.

$Fe_3O_4$ forms quickly under aqueous conditions, while $Fe_2O_3$ is undetected in as-grown $Fe_3O_4$ products. Nonetheless, $Fe_2O_3$ can be obtained by further aeration plus heating (99–101). During the geological processing of ultramafic rock, which is driven by aqueous fluids, $Fe_3O_4$, but not $Fe_2O_3$, is found as the secondary phase formed from the primary olivine mineral (15). Such

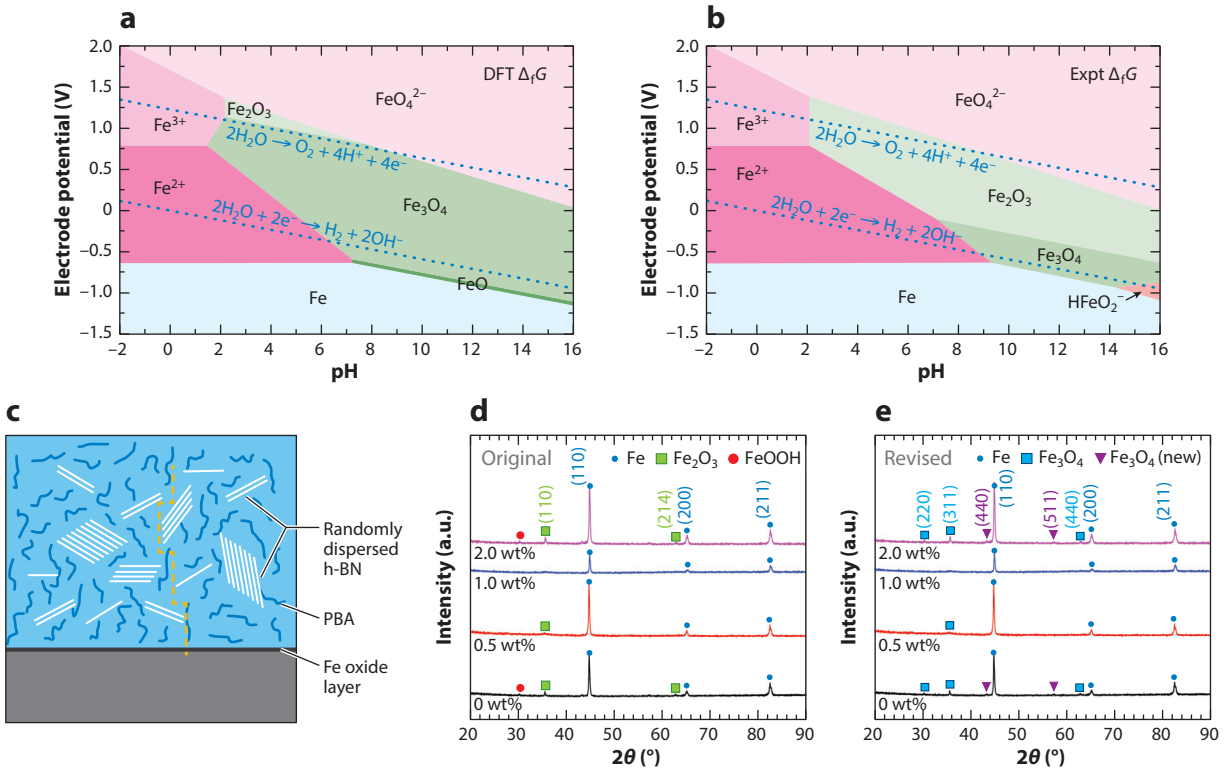


**Figure 6**

(*a*,*b*) Fe Pourbaix diagrams simulated using (*a*) density functional theory (DFT) and (*b*) experimental (expt) free energies of formation. Panels *a* and *b* adapted from Reference 96. (*c*) Schematics showing the experimental samples with a Fe oxide layer formed between a Fe metal substrate and epoxy coating [a compound with boron nitride (BN) and poly(2)butyl aniline (PBA)]. (*d*,*e*) The measured X-ray diffraction spectra for the corroded samples (BN contents at ∼0–2 wt% of the coatings) with the peaks (*d*) assigned in the original publication (98) and (*e*) revised here. Panels *c*–*e* adapted with permission from Reference 98. Copyright 2018, Elsevier B.V.

evidence in both electrochemical and geological fields supports the higher electrochemical stability of $Fe_3O_4$ relative to $Fe_2O_3$ as exhibited in the DFT-based Fe Pourbaix diagram in **Figure 6*a***. The well-known iron rust formed in humid environments (water plus air) usually consists of a hydrated form of $Fe_2O_3$, which may also indicate the relatively low stability of pristine $Fe_2O_3$ against structural defects when in contact with water. It has also been observed that $Fe_3O_4$ is stable at pH $\gtrsim$ 3.5 (99, 100, 102, 103), consistent with its dissolution boundaries at pH $\gtrsim$ 3.4 (at $U_p = 0$ V) for $[I] \lesssim 10^{-3}$ simulated using DFT $\Delta_f G$ values. In contrast, the experimental $\Delta_f G$ values lead to the dissolution boundaries of $Fe_3O_4$ at pH values of approximately 5.5 and greater (**Figure 6*b***), considerably deviating from the directly observed dependencies.

The DFT-based Fe Pourbaix diagrams can be used to reinterpret characterization results of recent experiments on Fe samples with corrosion-resistant polymer coatings (see the schematic in **Figure 6*c***) (97, 98). The corroded samples were characterized using XRD, and peaks in the XRD patterns were originally ascribed to the Fe substrate, $Fe_2O_3$, and FeOOH (**Figure 6*d***). According to the first-principles DFT-based Fe Pourbaix diagram, however, $Fe_3O_4$ should be the most stable oxide to form. Guided by this knowledge, one can examine the XRD patterns in detail for standard Fe metal, $Fe_2O_3$, $Fe_3O_4$, and FeOOH (104–106), and it is found that the XRD peaks in **Figure 6*d*** are better explained by the peak assignments assuming the presence of only Fe and $Fe_3O_4$. The

revised XRD interpretation is shown in **Figure 6*e***, where additional weak intensity peaks arising from $Fe_3O_4$ are now indicated. The oxide layer still plays an important role in the corrosion resistance of coated Fe (97, 98), and a precise understanding of its composition will be especially helpful for further optimizing the corrosion resistance of Fe-based structural materials.

## 4. ELECTROCHEMICAL PHASE DIAGRAMS OF DEFECTIVE SYSTEMS

Apart from the pristine bulk systems discussed above, there are many defective materials consisting of surfaces and point defects, and these low-dimensional defects are intimately involved in the electrochemical behaviors (active mechanisms) of realistic materials. The control of these defects is also a critical factor to consider when optimizing the corrosion resistance of materials. As an atomistic simulation tool, DFT is an effective approach to disentangle the multiple microscopic processes underlying an electrochemical behavior, because it can effectively integrate out degrees of freedom. To that end, DFT studies are important for making progress in understanding the complex phenomena of corrosion, with the aim of making useful composition-structure-stability relationships. Here we highlight advances in the development and application of DFT methods for calculating and understanding the electrochemical stabilities of surfaces, adsorbates on surfaces, and point defects.

### 4.1. Surface Systems

The interaction of materials with their environments occurs at surfaces, and many chemical/physical processes happening at surfaces (e.g., molecule dissociation, atom/molecule adsorption, surface dissolution, and defect diffusion) are of importance for various materials applications (9, 14, 23, 26, 28, 29, 107–109). Surface parameters such as morphology and adsorption play important roles in the oxidation (at high temperature) and corrosion (subject to electrochemical environments) of materials. In contrast, the state of the surface is determined by the intrinsic microscopic interactions and extrinsic environmental factors.

The Pourbaix diagrams for surface systems were first established by Marcus & Protopopoff (110–112), who used the measured thermodynamic energies to simulate the Pourbaix diagrams of S and O adsorbates on various metal surfaces (e.g., Cr, Fe, and Ni). Later, Taylor et al. (113) used DFT to calculate the reaction energies of $H_2O$, OH, H, and O adsorbates on Cu nanoparticles and surfaces, from which the nanoscale effect on the electrochemical stability of Cu against corrosion and passivation was derived. In addition, DFT-based surface Pourbaix diagrams have been constructed by Hansen et al. (114), who considered O, H, and OH adsorbates on the surfaces of Ag, Pt, and Ni, as these metals represent a class of superior catalysts.

The calculations of the necessary reaction chemical potentials ($\Delta\mu$) for the aforementioned simulations can be exemplified by a reaction path involving the OH adsorbate

$$H_2O + s \rightarrow HO{\cdot}s + H^+ + e^-,$$

where $s$ and $HO{\cdot}s$ represent the surface without and with the HO adsorbate, respectively. There are many surface parameters—e.g., crystalline orientation, geometry, vacancy, impurity, and adsorption—that can be considered and represented by $s$ here. For that reason, multiple surface Pourbaix diagrams can be computed to assess the most important surface features affecting electrochemical phase stability. The corresponding $\Delta\mu$ is expressed as

$$\Delta\mu = \mu_{HO} - \mu_{H_2O} - eU_p - k_B T \ln(10) \cdot \text{pH},$$

where the chemical potential (free energy of formation) of the HO adsorbate is calculated as

$$\mu_{HO} = E_e(HO{\cdot}s) - E_e(s) - \frac{1}{2}E_e(H_2) - \frac{1}{2}E_e(O_2) + \Delta_T,$$

where $E_e$ is the electronic energy obtained using DFT and a suitable exchange-correlation functional. The parameter $\Delta_T$ is the thermal energetic correction due to the atomic vibrations and molecular translations and rotations at finite temperatures (e.g., 25°C) (95). Similar reaction chemical potentials as before, i.e., those dependent on pH and/or $U_p$, were then established for all of the considered adsorbates at different coverages and were used to generate, for example, the Pourbaix diagrams for the adsorbates on Ag, Pt, and Ni surfaces (114). These surface Pourbaix diagrams can predict the type and optimal coverage of the most stable adsorbate at any specified electrochemical condition. Such knowledge is powerful because surface adsorption is the precursor for many ensuing reactions, including water electrolysis, oxidation, dissolution, and impurity/metal diffusion; therefore, the differences in adsorbate type and coverage may result in completely different active microscopic mechanisms governing the corrosion processes.

Persson et al. (53) also established a DFT method to calculate Pourbaix diagrams for nanoparticles (using Pt as an example) with adsorbates (e.g., O and OH), as shown in **Figure 7*a***. This approach makes it possible to predict multiple electrochemical properties of nanoparticles by using a single Pourbaix diagram; such properties include the most stable adsorbate, the optimal adsorbate coverage, the possible nanoparticle morphology, and the particle-size dependent stability. The information gained from the DFT-based nanoparticle Pourbaix diagrams is especially useful for the design, synthesis, and application of related nanoparticles (93, 94). In addition, on the basis of the reaction of the $LiFePO_4$ surface with solution as in lithium exchange, Persson et al. (53) also calculated the evolution of particle morphology with the chemical potential of oxygen ($\mu_O$;

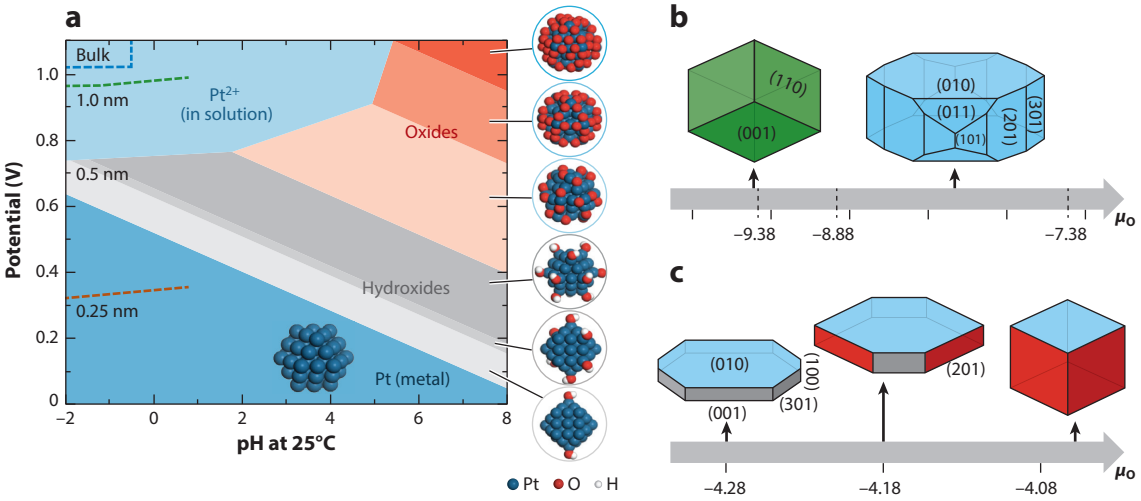


**Figure 7**

(*a*) Pourbaix diagram for Pt nanoparticles with O and OH adsorbates (at room temperature and $[Pt^{2+}] = 10^{-6}$ M). The Pt, O, and H atoms are represented by the blue (largest), red (medium), and white (smallest) spheres, respectively. (*b*,*c*) The evolution in $LiFePO_4$ particle morphology at different oxygen chemical potentials. The surfaces with adsorbates of H, $H_2O$, OH, and $O_2$ are indicated by green, blue, gray, and red, respectively. Here, the electronic energies are calculated using the density functional theory (DFT) + *U* method, with the vibrational free energies omitted for simplicity. Adapted with permission from Reference 53. Copyright 2012, American Physical Society.

depends on pH, as determined from Equation 1), as shown in **Figure 7*b***. The use of theory with these model simulations is useful for predicting the catalytic, corrosion, and oxidation behaviors of realistic samples, because different crystalline facets of solids often exhibit dramatically different surface reactivities and interactions with environmental factors such as water. Indeed, the DFT work on ZnO surfaces by Yoo et al. (115) is an important example of these dependencies. These authors demonstrate that water has a strong stabilizing effect on the polarized surfaces of the material. Furthermore, the potentiostat condition can be explicitly considered in the electrochemical simulations using DFT (116), which is useful for studying surface electrochemical phenomena far from equilibrium-like boundary conditions in materials that are sensitive to electric fields.

## 4.2. Point Defects

Metals in service are usually protected from extended oxidation and corrosion by the oxide layers that spontaneously form on the surfaces, and the mass transport across the oxide layer is responsible for both fast, early-stage (transient) oxidation and slow, late-stage oxidation (117–125). The oxide growth rate and morphology are closely dependent on the defects participating in the mass transport, and different types of migrating defects can result in different dynamical electric fields across the oxide layer that affect oxidation. For that reason, external voltages can strongly affect materials oxidation (126). Thus, to further optimize the corrosion resistance of functional metallic materials in realistic conditions, it is necessary both to identify the most probable defects migrating across the passivating oxide layer and to understand their kinetic dependencies.

The electronic structures, optical properties, and thermodynamic stabilities of defects in semiconductors have been intensively studied using DFT for decades (128–135). Recently, Todorova & Neugebauer further extended these defect theories to study corrosion (127, 136, 137). The free energy of formation ($\Delta_f G$) for a charged defect ($D^q$, where $q$ is its charge) is expressed as (127)

$$\Delta_f G(D^q) \approx \Delta_f E_e(D^q) = E_e(D^q : \text{host}) - E_e(\text{host}) - \sum_i \Delta n_i \mu_i + qE_F,$$

where $\Delta_f G$ is approximated by $\Delta_f E_e$ for simplicity, $\Delta n_i$ is the change in the number of the $i$ atomic species involved in the defect generation and $\mu_i$ is its chemical potential in the reservoir, and $E_F$ is the Fermi level indicating the electronic chemical potential of the electronic reservoir.

Panels *a* and *b* of **Figure 8** show the $\Delta_f G$ variations for the defects in ZnO with respect to $E_F$ in Zn-rich conditions [with $\mu_O = \Delta_f E_e(\text{ZnO}) - \mu^0_{Zn}$] and O-rich conditions [with $\mu_{Zn} = \Delta_f E_e(\text{ZnO}) - 0.5\mu^0_{O_2}$], from which the most stable defects can be identified at each given condition. The electrochemical phase diagram for the stable defects with respect to $E_F$ and $\mu_O$ are shown in **Figure 8*c***, which may be called a defect Pourbaix diagram because $E_F$ can be controlled by electrode potential and $\mu_O$ is proportional to the solution pH given by Equation 1. In the ZnO defect Pourbaix diagram, neutral oxygen vacancies, $V^0_O$, are found to be the most stable defect at low $\mu_O$ (e.g., at the metal–oxide interface), whereas charged zinc vacancies $V^{2-}_{Zn}$ (with neutral oxygen interstitials, $O^0_i$) are found to be the most stable (secondary) defects at high $\mu_O$ (e.g., at the oxide–electrolyte interface). Naturally, one would anticipate that, for example, a doubly negatively charged oxygen vacancy, $V^{2+}_O$, would mediate oxidation in electrochemically formed ZnO films (the conventional view); however, these calculations support the finding that other defects—including oxygen interstitials, $O^0_i$, or neutral oxygen vacancies, $V^0_O$ (the revised view)—are crucial for providing mass transport during oxidation of Zn. These conclusions based upon first-principles defect Pourbaix diagrams are helping to revise the current understanding of mass transport in ZnO thin films on Zn metal substrates (**Figure 8*d*,*e***), indicating the utility of defect Pourbaix diagrams for studying corrosion.

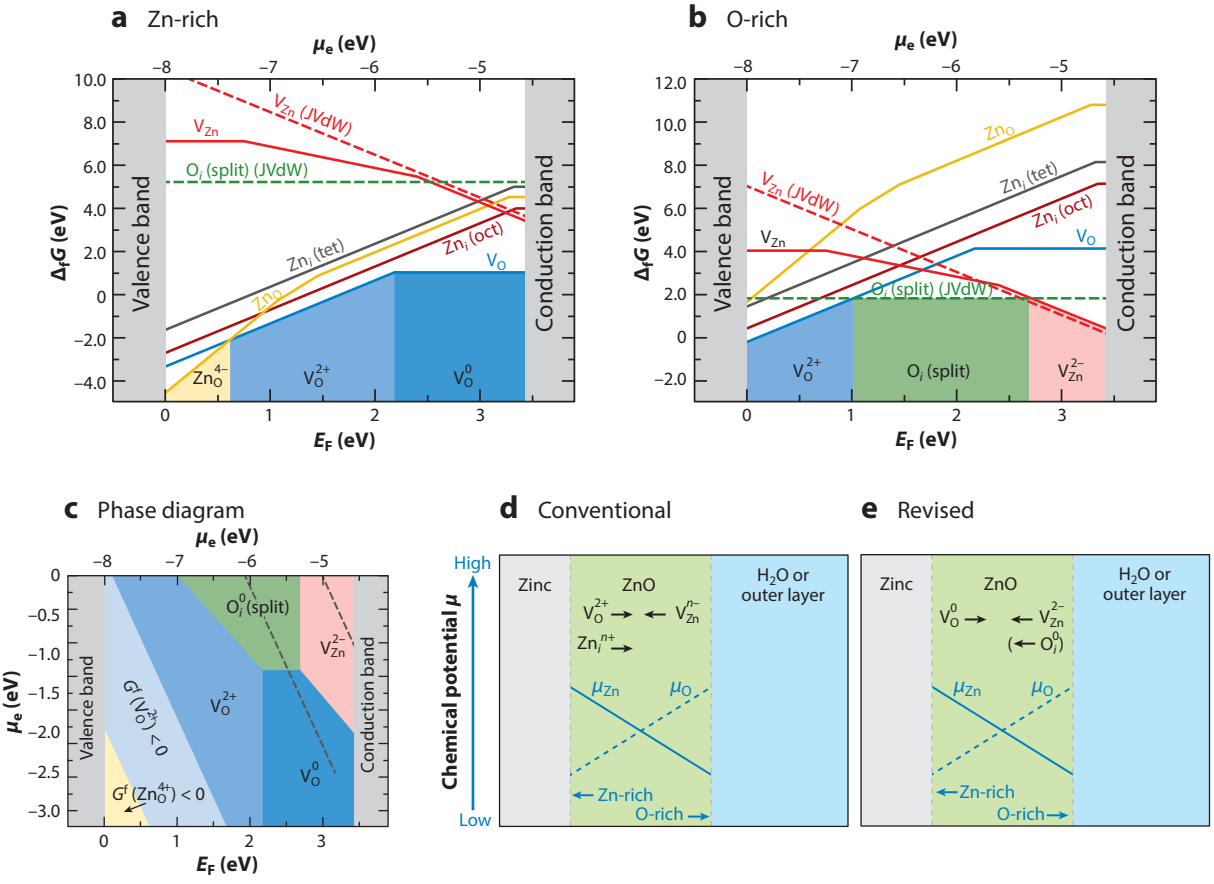


**Figure 8**

(*a*,*b*) Formation energies of point defects in ZnO in (*a*) Zn-rich and (*b*) O-rich conditions. (*c*) Electrochemical phase diagrams of point defects in ZnO with respect to Fermi level $E_F$ (or electron chemical potential $\mu_e$) and oxygen chemical potential $\mu_O$. (*d*) Conventional and (*e*) revised microscopic mechanisms for mass transport during the growth of the passivating zinc oxide layer. Here the electronic energies and band structures are calculated at the DFT-HSE (density functional theory–Heyd-Scuseria-Ernzerhof with screened Hartree-Fock exchange) level, with the vibrational free energies omitted for simplicity. Adapted with permission from Reference 127. Copyright 2015, The Royal Society of Chemistry.

Apart from point defects, there exist many other complex/extended defect structures, as well as the ubiquitous couplings between different defects (107, 108, 138, 139), for which the promising applications of defect Pourbaix diagrams can be expected. In addition, the simulation method can be readily transferred to study defect stability in other environmental conditions, e.g., dry atmosphere. To realize functional properties in ceramic materials, the type and concentration of defects have been controlled by tuning the electrode potential and atmospheric $p(O_2)$ (140, 141), in which context the theoretical simulation requires a similar physical picture as that for defect Pourbaix diagrams.

## 5. CONCLUSION

Corrosion has always been and will continue to be ubiquitous in our world and important in fields of science and engineering. Electrochemical phase diagrams are an effective tool for

understanding the thermodynamics of materials associated with corrosion and will continue to become more powerful in the future for materials design and disentangling complex mechanisms when computed using electronic structure methods. Above we review the basic principles of electrochemical phase diagrams of materials and the application of DFT to their construction. We emphasize that the recent developments of state-of-the-art first-principles methods now make it possible to simulate electrochemical phase diagrams of both model systems (pristine bulk materials) and realistic materials (those with surfaces, surface adsorbates, and point defects).

First-principles electrochemical phase diagrams can be utilized to solve problems where there is ambiguity in interpretation, for example, when the experimental complexity and dynamics of the system during corrosion or oxidation can lead to multiple equivalent semiempirical models. This is often the scenario present experimentally, as corrosion problems involve diverse materials phases and various microscopic events occurring at multiple spatial and temporal scales. Beyond applications in pure water, $O_2$, and $H_2$, many other environmental agents—e.g., dissolved $CO_2$, $H_2S$, $Cl^-$, and organics—may interact with the solids and be relevant to the concerned corrosion problems. Such intrinsic complexity to corrosion imposes a high-standard requirement on the accuracy and capability of the first-principles methods used to model these responses. We hope that the recent first-principles achievements reviewed here motivate the development of more state-of-the-art electronic structure methods and their application for understanding materials corrosion.

## FUTURE ISSUES

1. Complex compositions of materials: Many alloys and transition metal compounds exhibit intriguing physical and chemical properties (55, 125, 142–147), which arise from complex interactions among the constituent elements. The result is that multiple known or unknown nonequilibrium compositions and structures can form in a material during its lifetime, and those phases will respond differently to the environmental factors controlling corrosion. At present, it is challenging to simultaneously and accurately simulate all of the relevant phases, as well as the interactions/transitions between them, to discern the main mechanisms involved in corrosion. To that end, applying and advancing first-principles approaches that can navigate and model such complex compositional and structural phase spaces are of interest for making progress in the corrosion science domain.
2. Complex compositions of solutions: The aqueous electrolytes in contact with materials usually have complex compositions, and the electrochemical properties of metallic/compound materials may sensitively depend on the solution composition. Many gases (e.g., $O_2$, $H_2$, $CO_2$, and $H_2S$), $Cl^-$ and $Cl^-$-containing species, and organics (e.g., sugars, proteins, and contaminants) may be dissolved in various aqueous solutions (e.g., seawater, domestic water supplies, bodily fluids, and electrolytes for energy devices/facilities). Appropriate and accurate DFT methods are required to calculate the complicated interactions of these solution species with the targeted functional materials, as well as to generate useful electrochemical phase diagrams reflecting these important interactions. The related physical pictures established here can also be transferred to study many other complex environmental systems, e.g., nonaqueous battery electrolytes, ionic liquids, and molten salts at high temperatures.

3. Complex structural architectures: Realistic corrosion problems frequently involve materials with diverse nanoscale morphologies (26–29, 148). Heterogeneous nanoscale architectures may lead to new roles and dramatically unexpected behaviors of defects, interfaces, and surface adsorbates. To simulate such cases, the construction of plausible models, the achievement of high simulation accuracy for large systems, and the huge computational expense are foreseeable challenges.
4. Variable temperatures: Electrochemical stabilities of solid and aqueous systems at different temperatures can find considerable direct uses in many fields, e.g., ocean materials for global climates. For solids, there have been many advances in DFT methods for treating thermodynamic properties, although high-order anharmonicities still remain expensive to calculate (149). For aqueous systems, feasible methods, especially those that can obtain accurate quantities that can be directly used to explain and design experiments, are still lacking. Similar simulation methods or physical pictures established here will also be useful for many other fields with high temperatures, e.g., superior molten salts in extreme environments, next-generation nuclear reactors, and corrosion resistance of gas turbines against exhaust products.
5. Complex electronic physics: Rare-earth systems have numerous superior physical properties and are important additives to a wide variety of materials. However, the unique $f$ orbital atomic physics lead to extremely complex electronic exchange and correlation (150). Many successful applications of DFT (150, 151) and beyond approaches should be further extended to treat materials for electrochemical purposes.
6. Beyond electrochemical diagrams to kinetics: In experiments, there are always variable scales in time (e.g., from seconds to years) and space (e.g., from bulk down to subnanometers). The corrosion behaviors may then be largely influenced or even determined by many complex and joint kinetic processes with multiple temporal and spatial scales. Examples in this context include diffusion and phase transitions in metals and oxides; reactions at the metal–oxide, metal–electrolyte, and oxide–electrolyte interfaces; and ion/molecule mobility and transformations in aqueous solutions, for which DFT may need to combine with other models [e.g., the kinetic Monte Carlo method (28)] for effective simulations. Constructing appropriate physical models and performing accurate and efficient computations are quite challenging. In addition, reliable Pourbaix diagrams can provide very critical thermodynamic information (e.g., about the most important compounds, surfaces, adsorbates, and defects), which may substantially help avoid the simulation of unimportant kinetic steps.



## DISCLOSURE STATEMENT

The authors are not aware of any affiliations, memberships, funding, or financial holdings that might be perceived as affecting the objectivity of this review.

## ACKNOWLEDGMENTS

The authors were supported by the Office of Naval Research Multidisciplinary University Research Initiatives under grant N00014-16-1-2280 (“Understanding Atomic Scale Structure in Four Dimensions to Design and Control Corrosion Resistant Alloys”).

## LITERATURE CITED


1. Leyens C, Peters M. 2003. *Titanium and Titanium Alloys: Fundamentals and Applications*. Weinheim, Ger.: Wiley-VCH
2. Argon AS. 2008. *Strengthening Mechanisms in Crystal Plasticity*. New York: Oxford Univ. Press
3. Gupta M, Sharon NML. 2011. *Magnesium, Magnesium Alloys, and Magnesium Composites*. Hoboken, NJ: John Wiley & Sons
4. Niinomi M, Nakai M, Hieda J. 2012. Development of new metallic alloys for biomedical applications. *Acta Biomater.* 8:3888–903
5. Kudo A, Miseki Y. 2009. Heterogeneous photocatalyst materials for water splitting. *Chem. Soc. Rev.* 38:253–78
6. Wang G, Zhang L, Zhang J. 2012. A review of electrode materials for electrochemical supercapacitors. *Chem. Soc. Rev.* 41:797–828
7. Trotochaud L, Young SL, Ranney JK, Boettcher SW. 2014. Nickel-iron oxyhydroxide oxygen-evolution electrocatalysts: the role of intentional and incidental iron incorporation. *J. Am. Chem. Soc.* 136:6744–53
8. Burke MS, Zou S, Enman LJ, Kellon JE, Gabor CA, et al. 2015. Revised oxygen evolution reaction activity trends for first-row transition-metal (oxy)hydroxides in alkaline media. *J. Phys. Chem. Lett.* 6:3737–42
9. Hellman A, Wang B. 2017. First-principles view on photoelectrochemistry: water-splitting as case study. *Inorganics* 5:37
10. Syrett BC, Acharya A. 1979. *Corrosion and Degradation of Implant Materials*. Philadelphia: Am. Soc. Test. Mater.
11. Davis JR. 2000. *Corrosion: Understanding the Basics*. Materials Park, OH: ASM Int.
12. Grunette DM, Tengval P, Textor M, Thomsen P. 2001. *Titanium in Medicine: Material Science, Surface Science, Engineering, Biological Responses and Medical Applications*. Berlin: Springer
13. Scully JR. 2015. Corrosion chemistry closing comments: opportunities in corrosion science facilitated by operando experimental characterization combined with multi-scale computational modelling. *Faraday Discuss.* 180:577–93
14. Esmaily M, Svensson JE, Fajardo S, Birbilis N, Frankel GS, et al. 2017. Fundamentals and advances in magnesium alloy corrosion. *Prog. Mater. Sci.* 89:92–193
15. Beinlich A, Austrheim H, Mavromatis V, Grguric B, Putnis CV, Putnis A. 2018. Peridotite weathering is the missing ingredient of Earth's continental crust composition. *Nat. Commun.* 9:634
16. Hou B, Li X, Ma X, Du C, Zhang D, et al. 2017. The cost of corrosion in China. *NPJ Mater. Degrad.* 1:4
17. Clarivate Analytics. 2018. *Web of knowledge*. **https://clarivate.com/products/web-of-science/**
18. United Nations. 2017. *World population ageing 2017*. Rep., United Nations
19. Hoar TP, Mears DC. 1966. Corrosion-resistant alloys in chloride solutions: materials for surgical implants. *Proc. R. Soc. A Math. Phys. Eng. Sci.* 294:486–510
20. Pourbaix M. 1984. Electrochemical corrosion of metallic biomaterials. *Biomaterials* 5:122–34
21. Jacobs JJ, Gilbert JL, Urban RM. 1998. Current concepts review—corrosion of metal orthopaedic implants. *J. Bone Joint Surg.* 80:268–82
22. Han Y, Hong SH, Xu K. 2003. Structure and in vitro bioactivity of titania-based films by micro-arc oxidation. *Surf. Coat. Technol.* 168:249–58
23. Liu X, Chu PK, Ding C. 2004. Surface modification of titanium, titanium alloys, and related materials for biomedical applications. *Mater. Sci. Eng. R* 47:49–121
24. Geetha M, Singh AK, Asokamani R, Gogia AK. 2009. Ti based biomaterials, the ultimate choice for orthopaedic implants—a review. *Prog. Mater. Sci.* 54:397–425
25. Banerjee D, Williams JC. 2013. Perspectives on titanium science and technology. *Acta Mater.* 61:844–79
26. Frankel GS. 1998. Pitting corrosion of metals: a review of the critical factors. *J. Electrochem. Soc.* 145:2186–98
27. Marks L. 2018. Competitive chloride chemisorption disrupts hydrogen bonding networks: DFT, crystallography, thermodynamics, and morphological consequences. *Corrosion* 74:295–311

28. Taylor CD, Marcus P. 2015. *Molecular Modeling of Corrosion Processes*. Hoboken, NJ: John Wiley & Sons
29. Maurice V, Marcus P. 2018. Progress in corrosion science at atomic and nanometric scales. *Prog. Mater. Sci.* 95:132–71
30. Pourbaix M. 1966. *Atlas of Electrochemical Equilibria in Aqueous Solutions*. Oxford, UK: Pergamon Press
31. Beverskog B, Puigdomenech I. 1996. Revised Pourbaix diagrams for iron at 25–300°. *Corros. Sci.* 38:2121–35
32. Beverskog B, Puigdomenech I. 1997. Revised Pourbaix diagrams for nickel at 25–300°. *Corros. Sci.* 39:969–80
33. Beverskog B, Puigdomenech I. 1997. Revised Pourbaix diagrams for chromium at 25–300°C. *Corros. Sci.* 39:43–57
34. Muñoz-Portero MJ, García-Antón J, Guiñón JL, Pérez-Herranz V. 2007. Pourbaix diagrams for nickel in concentrated aqueous lithium bromide solutions at 25°C. *Corrosion* 63:625–34
35. Muñoz Portero MJ, García-Antón J, Guiñón JL, Leiva-García R. 2011. Pourbaix diagrams for titanium in concentrated aqueous lithium bromide solutions at 25°C. *Corros. Sci.* 53:1440–50
36. Cook WG, Olive RP. 2012. Pourbaix diagrams for the nickel-water system extended to high-subcritical and low-supercritical conditions. *Corros. Sci.* 58:284–90
37. Nickchi T, Alfantazi A. 2013. Potential-temperature (*E–T*) diagrams for iron, nickel, and chromium in sulfate solutions up to 473 K. *Electrochim. Acta* 104:69–77
38. Santucci RJ, McMahon ME, Scully JR. 2018. Utilization of chemical stability diagrams for improved understanding of electrochemical systems: evolution of solution chemistry towards equilibrium. *NPJ Mater. Degrad.* 2:1
39. Morel F, Morgan J. 1972. A numerical method for computing equilibria in aqueous chemical systems. *Environ. Sci. Technol.* 6:58–67
40. Bard AJ, Faulkner LR. 2000. *Electrochemical Methods: Fundamentals and Applications*. New York: John Wiley & Sons. 2nd ed.
41. Huang LF, Rondinelli JM. 2015. Electrochemical phase diagrams for Ti oxides from density functional calculations. *Phys. Rev. B* 92:245126
42. Van de Walle CG, Neugebauer J. 2003. Universal alignment of hydrogen levels in semiconductors, insulators and solutions. *Nature* 423:626–28
43. Alkauskas A, Broqvist P, Pasquarello A. 2008. Defect energy levels in density functional calculations: alignment and band gap problem. *Phys. Rev. Lett.* 101:046405
44. Cheng J, Sprik M. 2012. Alignment of electronic energy levels at electrochemical interfaces. *Phys. Chem. Chem. Phys.* 14:11245–67
45. Chen S, Wang LW. 2012. Thermodynamic oxidation and reduction potentials of photocatalytic semiconductors in aqueous solution. *Chem. Mater.* 24:3659–66
46. Cheng J, VandeVondele J. 2016. Calculation of electrochemical energy levels in water using the random phase approximation and a double hybrid functional. *Phys. Rev. Lett.* 116:086402
47. Pham TA, Ping Y, Galli G. 2017. Modelling heterogeneous interfaces for solar water splitting. *Nat. Mater.* 16:401–8
48. Huang LF, Hutchison MJ, Santucci RJ, Scully JR, Rondinelli JM. 2017. Improved electrochemical phase diagrams from theory and experiment: the Ni-water system and its complex compounds. *J. Phys. Chem. C* 121:9782–89
49. Chen BR, Sun W, Kitchaev DA, Mangum JS, Thampy V, et al. 2018. Understanding crystallization pathways leading to manganese oxide polymorph formation. *Nat. Commun.* 9:2553
50. Chivot J, Mendoza L, Mansour C, Pauporté T, Cassir M. 2008. New insight in the behaviour of Co-$H_2O$ system at 25–150°C, based on revised Pourbaix diagrams. *Corros. Sci.* 50:62–69
51. Cook WG, Olive RP. 2012. Pourbaix diagrams for the iron-water system extended to high-subcritical and low-supercritical conditions. *Corros. Sci.* 55:326–31
52. Cook WG, Olive RP. 2012. Pourbaix diagrams for chromium, aluminum and titanium extended to high-subcritical and low-supercritical conditions. *Corros. Sci.* 58:291–98
53. Persson KA, Waldwick B, Lazic P, Ceder G. 2012. Prediction of solid-aqueous equilibria: scheme to combine first-principles calculations of solids with experimental aqueous states. *Phys. Rev. B* 85:235438

54. Zinkle SJ, Snead LL. 2014. Designing radiation resistance in materials for fusion energy. *Annu. Rev. Mater. Res.* 44:241–67
55. Rondinelli JM, Kioupakis E. 2015. Predicting and designing optical properties of inorganic materials. *Annu. Rev. Mater. Res.* 45:491–518
56. Samsonov GV. 1973. *The Oxide Handbook*. New York: IFI/Plenum Press
57. Burgess J. 1978. *Metal Ions in Solution*. Chichester, UK: Ellis Horwood
58. Bard AJ, Parsons R, Jordan J. 1985. *Standard Potentials in Aqueous Solution*. New York: Marcel Dekker
59. Kubaschewski O, Alcock CB, Spencer PJ. 1993. *Materials Thermochemistry*. Oxford, UK: Pergamon Press
60. Chase MW. 1998. *NIST-JANAF Thermochemical Tables*. New York: Am. Inst. Phys. 4th ed.
61. Mochizuki S, Saito T. 2009. Intrinsic and defect-related luminescence of NiO. *Physica B* 404:4850–53
62. Hohenberg P, Kohn W. 1964. Inhomogeneous electron gas. *Phys. Rev.* 136:B864–71
63. Kohn W, Sham LJ. 1965. Self-consistent equations including exchange and correlation effects. *Phys. Rev.* 140:A1133–38
64. Martin RM. 2004. *Electronic Structure: Basic Theory and Practical Methods*. Cambridge, UK: Cambridge Univ. Press
65. Jones RO, Gunnarsson O. 1989. The density functional formalism, its applications and prospects. *Rev. Mod. Phys.* 61:689–746
66. Jones RO. 2015. Density functional theory: its origins, rise to prominence, and future. *Rev. Mod. Phys.* 87:897–923
67. Ceperley DM, Alder BJ. 1980. Ground state of the electron gas by a stochastic method. *Phys. Rev. Lett.* 45:566–69
68. Perdew JP, Zunger A. 1981. Self-interaction correction to density-functional approximations for many-electron systems. *Phys. Rev. B* 23:5048–79
69. Perdew JP, Burke K, Ernzerhof M. 1996. Generalized gradient approximation made simple. *Phys. Rev. Lett.* 77:3865–68
70. Perdew JP, Ruzsinszky A, Csonka GI, Vydrov OA, Scuseria GE, et al. 2008. Restoring the density-gradient expansion for exchange in solids and surfaces. *Phys. Rev. Lett.* 100:136406
71. Tao J, Perdew JP, Staroverov VN, Scuseria GE. 2003. Climbing the density functional ladder: nonempirical meta–generalized gradient approximation designed for molecules and solids. *Phys. Rev. Lett.* 91:146401
72. Perdew JP, Ruzsinszky A, Csonka GI, Constantin LA, Sun J. 2009. Workhorse semilocal density functional for condensed matter physics and quantum chemistry. *Phys. Rev. Lett.* 103:026403
73. Sun J, Haunschild R, Xiao B, Bulik IW, Scuseria GE, Perdew JP. 2013. Semilocal and hybrid meta-generalized gradient approximations based on the understanding of the kinetic-energy-density dependence. *J. Chem. Phys.* 138:044113
74. Sun J, Ruzsinszky A, Perdew JP. 2015. Strongly constrained and appropriately normed semilocal density functional. *Phys. Rev. Lett.* 115:036402
75. Becke AD. 1993. A new mixing of Hartree-Fock and local density-functional theories. *J. Chem. Phys.* 98:1372–77
76. Paier J, Marsman M, Kresse G. 2007. Why does the B3LYP hybrid functional fail for metals?. *J. Chem. Phys.* 127:024103
77. Perdew JP, Ernzerhof M, Burke K. 1996. Rationale for mixing exact exchange with density functional approximations. *J. Chem. Phys.* 105:9982–85
78. Heyd J, Scuseria GE, Ernzerhof M. 2003. Hybrid functionals based on a screened Coulomb potential. *J. Chem. Phys.* 118:8207–15
79. Heyd J, Scuseria GE, Ernzerhof M. 2006. Erratum: "Hybrid functionals based on a screened Coulomb potential" [J. Chem. Phys. 118, 8207 (2003)]. *J. Chem. Phys.* 124:219906
80. Vydrov OA, Heyd J, Krukau AV, Scuseria GE. 2006. Importance of short-range versus long-range Hartree-Fock exchange for the performance of hybrid density functionals. *J. Chem. Phys.* 125:074106
81. Paier J, Marsman M, Hummer K, Kresse G, Gerber IC, Ángyán JG. 2006. Screened hybrid density functionals applied to solids. *J. Chem. Phys.* 124:154709

82. Mardirossian N, Head-Gordon M. 2017. Thirty years of density functional theory in computational chemistry: an overview and extensive assessment of 200 density functionals. *Mol. Phys.* 115:2315–72
83. Su NQ, Xu X. 2017. Development of new density functional approximations. *Annu. Rev. Phys. Chem.* 68:155–82
84. Anisimov VI, Aryasetiawan F, Lichtenstein AI. 1997. First-principles calculations of the electronic structure and spectra of strongly correlated systems: the LDA+*U* method. *J. Phys. Condens. Matter* 9:767–808
85. Campo VL Jr., Cococcioni M. 2010. Extended DFT+*U*+*V* method with on-site and inter-site electronic interactions. *J. Phys. Condens. Matter* 22:055602
86. Wang L, Maxisch T, Ceder G. 2006. Oxidation energies of transition metal oxides within the GGA + U framework. *Phys. Rev. B* 73:195107
87. Jain A, Hautier G, Ong SP, Moore CJ, Fischer CC, et al. 2011. Formation enthalpies by mixing GGA and GGA+*U* calculations. *Phys. Rev. B* 84:045115
88. Lutfalla S, Shapovalov V, Bell AT. 2011. Calibration of the DFT/GGA+U method for determination of reduction energies for transition and rare earth metal oxides of Ti, V, Mo, and Ce. *J. Chem. Theory Comput.* 7:2218–23
89. Aykol M, Wolverton C. 2014. Local environment dependent GGA + *U* method for accurate thermochemistry of transition metal compounds. *Phys. Rev. B* 90:115105
90. Lany S. 2008. Semiconductor thermochemistry in density functional calculations. *Phys. Rev. B* 78:245207
91. Stevanovic V, Lany S, Zhang X, Zunger A. 2012. Correcting density functional theory for accurate predictions of compound enthalpies of formation: fitted elemental-phase reference energies. *Phys. Rev. B* 85:115104
92. Zeng Z, Chan MKY, Zhao ZJ, Kubal J, Fan D, Greeley J. 2015. Towards first principles–based prediction of highly accurate electrochemical Pourbaix diagrams. *J. Phys. Chem. C* 119:18177–87
93. Tang L, Li X, Cammarata RC, Friesen C, Sieradzki K. 2010. Electrochemical stability of elemental metal nanoparticles. *J. Am. Chem. Soc.* 132:11722–26
94. Tang L, Han B, Persson K, Friesen C, He T, et al. 2010. Electrochemical stability of nanometer-scale Pt particles in acidic environments. *J. Am. Chem. Soc.* 132:596–600
95. Huang LF, Rondinelli JM. 2017. Electrochemical phase diagrams of Ni from ab initio simulations: role of exchange interactions on accuracy. *J. Phys. Condens. Matter* 29:475501
96. Huang LF, Rondinelli JM. 2018. Reliable electrochemical phase diagrams of magnetic transition metals and related compounds from high-throughput *ab-initio* calculations. Submitted
97. Chen C, Qiu S, Cui M, Qin S, Yan G, et al. 2017. Achieving high performance corrosion and wear resistant epoxy coatings via incorporation of noncovalent functionalized graphene. *Carbon* 114:356–66
98. Cui M, Ren S, Qin S, Xue Q, Zhao H, Wang L. 2018. Processable poly(2-butylaniline)/hexagonal boron nitride nanohybrids for synergetic anticorrosive reinforcement of epoxy coating. *Corros. Sci.* 131:187–98
99. Kang YS, Risbud S, Rabolt JF, Stroeve P. 1996. Synthesis and characterization of nanometer-size $Fe_3O_4$ and $\gamma$-$Fe_2O_3$ particles. *Chem. Mater.* 8:2209–11
100. Jolivet JP, Chanéac C, Tronc E. 2004. Iron oxide chemistry. From molecular clusters to extended solid networks. *Chem. Commun.* 2004:481–83
101. Petcharoen K, Sirivat A. 2012. Synthesis and characterization of magnetite nanoparticles via the chemical co-precipitation method. *Mater. Sci. Eng. B* 177:421–27
102. Burke LD, Lyons MEG. 1986. The formation and stability of hydrous oxide films on iron under potential cycling conditions in aqueous solution at high pH. *J. Electroanal. Chem.* 198:347–68
103. Lee J, Isobe T, Senna M. 1996. Preparation of ultrafine $Fe_3O_4$ particles by precipitation in the presence of PVA at high pH. *J. Colloid Interface Sci.* 177:490–94
104. Han R, Li W, Pan W, Zhu M, Zhou D, Li FS. 2014. 1D magnetic materials of $Fe_3O_4$ and Fe with high performance of microwave absorption fabricated by electrospinning method. *Sci. Rep.* 4:7493
105. Wei Y, Ding R, Zhang C, Lv B, Wang Y, et al. 2017. Facile synthesis of self-assembled ultrathin $\alpha$-FeOOH nanorod/graphene oxide composites for supercapacitors. *J. Colloid Interface Sci.* 504:593–602
106. Song H, Xia L, Jia X, Yang W. 2018. Polyhedral $\alpha$-$Fe_2O_3$ crystals at RGO nanocomposites: synthesis, characterization, and application in gas sensing. *J. Alloys Compd.* 732:191–200

107. Padture NP, Gell M, Jordan EH. 2002. Thermal barrier coatings for gas-turbine engine applications. *Science* 296:280–84
108. Clarke DR, Levi CG. 2003. Materials design for the next generation thermal barrier coatings. *Annu. Rev. Mater. Res.* 33:383–417
109. Zeng Z, Chang KC, Kubal J, Markovic NM, Greeley J. 2017. Stabilization of ultrathin (hydroxy) oxide films on transition metal substrates for electrochemical energy conversion. *Nat. Energy* 2:17070
110. Marcus P, Protopopoff E. 1990. Potential pH diagrams for adsorbed species: application to sulfur adsorbed on iron in water at 25° and 300°C. *J. Electrochem. Soc.* 137:2709–12
111. Marcus P, Protopopoff E. 1993. Potential pH diagrams for sulfur and oxygen adsorbed on nickel in water at 25 and 300°C. *J. Electrochem. Soc.* 140:1571–75
112. Marcus P, Protopopoff E. 1997. Potential pH diagrams for sulfur and oxygen adsorbed on chromium in water. *J. Electrochem. Soc.* 144:1586–90
113. Taylor CD, Neurock M, Scully JR. 2008. First-principles investigation of the fundamental corrosion properties of a model $Cu_{38}$ nanoparticle and the (111), (113) surfaces. *J. Electrochem. Soc.* 155:C407–14
114. Hansen HA, Rossmeisl J, Nørskov JK. 2008. Surface Pourbaix diagrams and oxygen reduction activity of Pt, Ag and Ni (111) surfaces studied by DFT. *Phys. Chem. Chem. Phys.* 10:3722–30
115. Yoo SH, Todorova M, Neugebauer J. 2018. Selective solvent-induced stabilization of polar oxide surfaces in an electrochemical environment. *Phys. Rev. Lett.* 120:066101
116. Surendralal S, Todorova M, Finnis MW, Neugebauer J. 2018. First-principles approach to model electrochemical reactions: understanding the fundamental mechanisms behind Mg corrosion. *Phys. Rev. Lett.* 120:246801
117. Cabrera N, Mott NF. 1949. Theory of the oxidation of metals. *Rep. Prog. Phys.* 12:163–84
118. Fehlner FP, Mott NF. 1970. Low-temperature oxidation. *Oxid. Met.* 2:59–99
119. Lawless KR. 1974. The oxidation of metals. *Rep. Prog. Phys.* 37:231–316
120. Chao CY, Lin LF, Macdonald DD. 1981. A point defect model for anodic passive films. I. Film growth kinetics. *J. Electrochem. Soc.* 128:1187–94
121. Atkinson A. 1985. Transport processes during the growth of oxide films at elevated temperature. *Rev. Mod. Phys.* 57:437–70
122. Macdonald DD. 1992. The point defect model for the passive state. *J. Electrochem. Soc.* 139:3434–49
123. Seyeux A, Maurice V, Marcus P. 2013. Oxide film growth kinetics on metals and alloys. I. Physical model. *J. Electrochem. Soc.* 160:C189–96
124. Leistner K, Toulemonde C, Diawara B, Seyeux A, Marcus P. 2013. Oxide film growth kinetics on metals and alloys. II. Numerical simulation of transient behavior. *J. Electrochem. Soc.* 160:C197–205
125. Yu X-x, Gulec A, Sherman Q, Cwalina KL, Scully JR, et al. 2018. Nonequilibrium solute capture in passivating oxide films. *Phys. Rev. Lett.* 121:145701
126. Heuer AH, Nakagawa T, Azar MZ, Hovis DB, Smialek JL, et al. 2013. On the growth of $Al_2O_3$ scales. *Acta Mater.* 61:6670–83
127. Todorova M, Neugebauer J. 2015. Identification of bulk oxide defects in an electrochemical environment. *Faraday Discuss.* 180:97–112
128. Laks DB, Van de Walle CG, Neumark GF, Pantelides ST. 1991. Role of native defects in wide-band-gap semiconductors. *Phys. Rev. Lett.* 66:648–51
129. Zhang SB, Northrup JE. 1991. Chemical potential dependence of defect formation energies in GaAs: application to Ga self-diffusion. *Phys. Rev. Lett.* 67:2339–42
130. Foster AS, Sulimov VB, Lopez Gejo F, Shluger AL, Nieminen RM. 2001. Structure and electrical levels of point defects in monoclinic zirconia. *Phys. Rev. B* 64:224108
131. Foster AS, Lopez Gejo F, Shluger AL, Nieminen RM. 2002. Vacancy and interstitial defects in hafnia. *Phys. Rev. B* 65:174117
132. Van de Walle CG, Neugebauer J. 2004. First-principles calculations for defects and impurities: applications to III-nitrides. *J. Appl. Phys.* 95:3851–79
133. Freysoldt C, Grabowski B, Hickel T, Neugebauer J, Kresse G, et al. 2014. First-principles calculations for point defects in solids. *Rev. Mod. Phys.* 86:253–305

134. Wu YN, Zhang XG, Pantelides ST. 2017. Fundamental resolution of difficulties in the theory of charged point defects in semiconductors. *Phys. Rev. Lett.* 119:105501
135. Dreyer CE, Alkauskas A, Lyons JL, Janotti A, Van de Walle CG. 2018. First-principles calculations of point defects for quantum technologies. *Annu. Rev. Mater. Res.* 48:1–26
136. Todorova M, Neugebauer J. 2014. Extending the concept of defect chemistry from semiconductor physics to electrochemistry. *Phys. Rev. Appl.* 1:014001
137. Todorova M, Neugebauer J. 2015. Connecting semiconductor defect chemistry with electrochemistry: impact of the electrolyte on the formation and concentration of point defects in ZnO. *Surf. Sci.* 631:190–95
138. Gritsenko VA, Perevalov TV, Islamov DR. 2016. Electronic properties of hafnium oxide: a contribution from defects and traps. *Phys. Rep.* 613:1–20
139. Gregori G, Merkle R, Maier J. 2017. Ion conduction and redistribution at grain boundaries in oxide systems. *Prog. Mater. Sci.* 89:252–305
140. Lu Q, Yildiz B. 2016. Voltage-controlled topotactic phase transition in thin-film $SrCoO_x$ monitored by in situ X-ray diffraction. *Nano Lett.* 16:1186–93
141. Lu N, Zhang P, Zhang Q, Qiao R, He Q, et al. 2017. Electric-field control of tri-state phase transformation with a selective dual-ion switch. *Nature* 546:124–28
142. Al-Hinai AT, Al-Hinai MH, Dutta J. 2014. Application of $E_h$–pH diagram for room temperature precipitation of zinc stannate microcubes in an aqueous media. *Mater. Res. Bull.* 49:645–50
143. Castelli IE, Thygesen KS, Jacobsen KW. 2014. Calculated Pourbaix diagrams of cubic perovskites for water splitting: stability against corrosion. *Top. Catal.* 57:265–72
144. Van der Ven A, Thomas JC, Puchala B, Natarajan AR. 2018. First-principles statistical mechanics of multicomponent crystals. *Annu. Rev. Mater. Res.* 48:27–55
145. Yeh JW, Chen SK, Lin SJ, Gan JY, Chin TS, et al. 2004. Nanostructured high-entropy alloys with multiple principal elements: novel alloy design concepts and outcomes. *Adv. Eng. Mater.* 6:299–303
146. Zhang Y, Zuo TT, Tang T, Gao MC, Dahmen KA, et al. 2014. Microstructures and properties of high-entropy alloys. *Prog. Mater. Sci.* 61:1–93
147. Qiu Y, Thomas S, Gibson MA, Fraser HL, Birbilis N. 2017. Corrosion of high entropy alloys. *NPJ Mater. Degrad.* 1:15
148. Frankel GS, Vienna JD, Lian J, Scully JR, Gin S, et al. 2018. A comparative review of the aqueous corrosion of glasses, crystalline ceramics, and metals. *NPJ Mater. Degrad.* 2:15
149. Huang LF, Lu XZ, Tennessen E, Rondinelli JM. 2016. An efficient ab-initio quasiharmonic approach for the thermodynamics of solids. *Comput. Mater. Sci.* 120:84–93
150. Moore KT, van der Laan G. 2009. Nature of the 5*f* states in actinide metals. *Rev. Mod. Phys.* 81:235–98
151. Wen XD, Martin RL, Henderson TM, Scuseria GE. 2013. Density functional theory studies of the electronic structure of solid state actinide oxides. *Chem. Rev.* 113:1063–96

Annual Review of
Materials Research

Volume 49, 2019

# Contents



## Computational Methods in Materials



## Topological Quantum Materials

## Current Interest



## Indexes



## Errata

An online log of corrections to *Annual Review of Materials Research* articles may be found at http://www.annualreviews.org/errata/matsci